

RESEARCH ARTICLE | SEPTEMBER 05 2024

Imaging nanoscale molecular binding in functionalized graphene via tip-enhanced Raman spectroscopy

Xiao You  ; Chiung-Wei Huang  ; Kizhanipuram Vinodgopal; Joanna M. Atkin  



J. Chem. Phys., 161, 094204 (2024)
<https://doi.org/10.1063/5.0222228>



View
Online



Export
Citation

Articles You May Be Interested In

X-ray nanospectroscopy for attogram-scale two-dimensional nanomaterials using photoelectron emission microscopy

AIP Conference Proceedings (June 2010)

Sharp, high numerical aperture (NA), nanoimprinted bare pyramid probe for optical mapping

Rev. Sci. Instrum. (March 2023)

Study of the modification of the hydrophobic properties of thin carbon films via thermo-assisted Tip-Enhanced Raman Scattering method

AIP Conf. Proc. (December 2020)

Imaging nanoscale molecular binding in functionalized graphene via tip-enhanced Raman spectroscopy

Cite as: J. Chem. Phys. 161, 094204 (2024); doi: 10.1063/5.0222228

Submitted: 6 June 2024 • Accepted: 19 August 2024 •

Published Online: 5 September 2024



View Online



Export Citation



CrossMark

Xiao You,^{1,2} Chiung-Wei Huang,³ Kizhanipuram Vinodgopal,⁴ and Joanna M. Atkin^{3,a}

AFFILIATIONS

¹ Department of Applied Physical Science, University of North Carolina at Chapel Hill, Chapel Hill, North Carolina 27599, USA

² Department of Engineering, Westlake University, Hangzhou, China

³ Department of Chemistry, University of North Carolina at Chapel Hill, Chapel Hill, North Carolina 27599, USA

⁴ Department of Chemistry, North Carolina Central University, Durham, North Carolina 27707, USA

^aAuthor to whom correspondence should be addressed: jatkin@email.unc.edu

ABSTRACT

Surface functionalization of low-dimensional nanomaterials offers a means to tailor their optoelectronic and chemical characteristics. However, functionalization reactions are sensitive to the inherent surface features of nanomaterials, such as defects, grain boundaries, and edges. Conventional optical characterization methods, such as Raman spectroscopy, have limited sensitivity and spatial resolution and, therefore, struggle to visualize reaction sites and chemical species. Here, we demonstrate the capability of spatially and chemically sensitive tip-enhanced Raman spectroscopy imaging to map the distribution of molecules in covalently functionalized graphene. Hyperspectral vertex component analysis and density functional theory are necessary to interpret the nature of binding sites and extract information from the spatially and spectrally heterogeneous datasets. Our results clarify the origin of heterogeneous surface functionalization, resolving preferential binding at edges and defects. This work demonstrates the potential of nanospectroscopic tools combined with unsupervised learning to characterize complex, partially ordered optoelectronic nanomaterials.

Published under an exclusive license by AIP Publishing. <https://doi.org/10.1063/5.0222228>

INTRODUCTION

Graphene's remarkable characteristics, such as its high carrier mobility and optical absorptivity, have led to its prominence in emerging devices and circuitry for the electronics industry.^{1,2} Many graphene-based devices, including gas sensors,^{3–5} biomedical devices,⁶ photonics,^{7,8} and electronic transistors,^{9,10} leverage these properties. The ability to functionalize graphene is crucial for tailoring its properties to specific applications, whether opening a bandgap or controlling optical and chemical characteristics. The desired electronic and optoelectronic properties in the functionalized graphene derivatives are governed by the nature and distribution of the introduced chemical species.^{11,12} For instance, the density of functionalization plays a crucial role in determining the degree of bandgap opening, as has been demonstrated by substitutional carbon-heteroatom (B, N, F, and Si atoms) binding.^{10,13–15} Post-grafting modification of graphene also showed

modulation of the band structure and bandgap.^{16,17} However, conventional strategies involving σ -bond forming reactions disrupt sp^2 conjugation and the associated continuum of delocalized π -electron clouds.^{18–21} The destructive rehybridization adversely affects the conductivity and mobility, thereby diminishing the desirable properties of graphene-based devices.²²

In contrast, interfacing the delocalized π electron with functional molecules through hexahapto (η^6) complexing functionalization retains the in-plane transport and sp^2 conjugation properties.^{23–26} The η^6 functionalization has the ability to serve as an electrical interconnect between carbon allotropes and metal nanoparticles.^{27,28} However, the large degree of inhomogeneity within these systems poses a significant challenge in terms of characterization. The morphological, chemical, and interfacial diversity complicates the comprehensive understanding of these functionalized structures. For example, intrinsic defects in graphene, such as atomic vacancies, wrinkles, ripples, and edges, theoretically

proposed as selective sites for chemical functionalization due to their heightened reactivity,^{29,30} have not yet been proven in experimental demonstration. The intricate nature of these systems and the lack of analytical tools make it difficult to showcase the selective reactivity of intrinsic defects in practice.

In this study, we use tip-enhanced Raman spectroscopy (TERS) to resolve site-specific chemical fingerprints on the surface of Cr(η^6 -C₆H₆) attached graphene, imaging functionalization density, and chemical structure. TERS combines ultrahigh spatial localization from scanning probe microscopy (SPM) and chemical specificity from Raman spectroscopy, which can overcome the diffraction limit of conventional optical spectroscopy. The highly confined and enhanced electromagnetic field generated within a plasmonic tip-surface cavity is capable of carrying local information about graphene and its defect sites that conventional optical spectroscopy lacks.³¹⁻³⁶ However, functionalized graphene and graphene-derived systems have not yet been extensively explored with TERS.^{32,37-39} In intrinsically disordered systems, mining structural information from TERS datasets can be challenging due to their large size and heterogeneity in spectral and spatial properties. We herein demonstrate a multivariate analysis framework using vertex component analysis (VCA) and hierarchical clustering analysis (HCA) to extract chemical information, facilitating visualization and interpretation of the nanoscale structure of molecules attached to a graphene film. The identification of the resulting vibrational Raman modes is validated through density functional theory (DFT). The model of Cr(η^6 -C₆H₆) anchored graphene demonstrates the nanoscale structure-property correlation for other disordered materials and allows us to confirm preferential binding at edge sites in the graphene lattice.

METHODS

Functionalized graphene preparation

The η^6 -Cr-benzene modified graphene that we study utilizes η^6 -functionalization to minimize disruption to the π -cloud continuum and is synthesized *in situ* using chemical vapor deposition (CVD). First, monolayer graphene was grown on a copper foil substrate. Then, the graphene surface was reacted *in situ* with the gas phase precursor (CO)₃-Cr-C₆H₆. The chromium-benzene complex (Cr-benzene) is attached to the graphene surface via hexahapto concomitant formation between chromium and graphene, producing (η^6 -graphene)Cr(η^6 -C₆H₆), as the reaction process shown in Fig. S1. The three carbonyl moieties detach from Cr and form carbon monoxide (CO) as a byproduct. Further detail on the reaction process is provided in the [supplementary material](#).

Tip-enhanced Raman spectroscopy

TERS measurements were performed on an AFM-Raman system comprising a scanning probe microscope (SmartSPM, AIST-NT) with a Raman spectrometer (LabRAM HR Evolution, Horiba Scientific) in side illumination geometry. A 633 nm HeNe excitation laser was focused on the sample using a 100 \times , 0.7 NA objective lens (Mitutoyo M Plan Apo) with the laser power lower than 0.5 mW at the sample. The TERS probes were prepared by sputtering (Kurt Lesker PVD 75 magnetron) 80 nm of gold on

silicon tips (ultrasharp noncontact NSC12/50, MikroMasch), which in combination with the gold substrate provided high enhancement for sensitive TERS. Each TERS spectrum was collected with 1 s accumulation.

DFT calculation

Density functional calculations were performed with the CASTEP module from Materials Studio 2019. The model geometry was optimized using the generalized gradient approximation (GGA) functional in the scheme of Perdew-Burke-Ernzerhof (PBE). An energy cutoff of 700 eV was used for the plane-wave basis. We have applied a slab approach with vacuum layers of 2 nm to decouple periodic images from each other along the z direction. Vibrational frequency calculations were carried out on the optimized geometry of functionalized graphene. All the calculations were performed using the computer cluster at the University of North Carolina Chapel Hill, USA.

RESULTS

We study hexahapto-functionalized graphene (η^6 -graphene)Cr(η^6 -C₆H₆), which minimizes disruption to the π -cloud continuum.⁴⁰ Previous studies have demonstrated the generation of this structure via wet-chemical processes, but this produces highly defective graphene with poor conductivity properties.^{23,27,41} In contrast, *in situ* functionalization of chemical vapor deposition (CVD) graphene, as utilized here, allows for short reaction times and contamination-free functionalization.^{14,28,42} The SEM measurements confirm that the morphology of graphene remains intact after CVD functionalization (Fig. S2). In addition, the EDX measurements verify the presence of chromium on the graphene surface (Fig. S3).

The presence of chromium atoms, whether physically adsorbed or chemically bonded, is expected to alter the Raman spectra of graphene, depending on the distribution of chromium across the surface. The Raman spectra of the pristine CVD graphene before reacting with precursor and the reacted product (η^6 -graphene)Cr(η^6 -C₆H₆) are shown in the [supplementary material](#), Fig. S4. The graphene spectra before and after functionalization are similar, exhibiting only the characteristic G, D, and 2D bands.⁴³ After functionalization, the D band appears but remains weak, suggesting that CVD functionalization of Cr(η^6 -C₆H₆) minimally disturbs the in-plane vibrational mode. In addition, the 2D band is redshifted and widened after the reaction, implying electron doping on graphene arising from functionalization.⁴⁴⁻⁴⁶ The Raman data also highlight the intrinsic limitations of conventional Raman spectroscopy in sensitivity and spatial resolution, making it insufficient to unequivocally identify functionalization.

Further characterization of the film was carried out using TERS mapping. [Figure 1\(c\)](#) shows a representative topographic map of the (η^6 -graphene)Cr(η^6 -C₆H₆) sample, acquired during TERS mapping. The AFM height image of 5 μ m by 5 μ m region reflects the surface roughness of the polycrystalline copper substrate. This roughness significantly influences the observed topography at the micrometer scale, as it causes variations in the height measurements that overshadow the actual thickness of the graphene layers. The AFM phase image provides additional information about the material

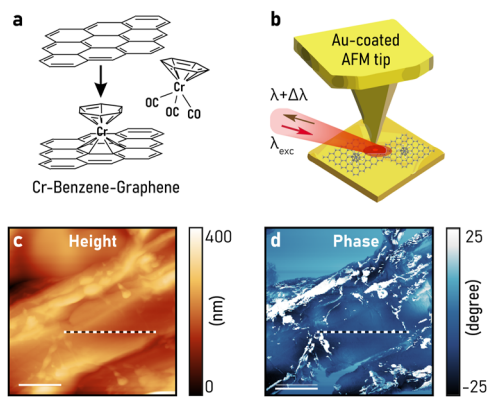


FIG. 1. Schematic illustration of the functionalization mechanism and experimental setup. (a) Chemical reaction of the precursor $(CO)_3$ -Cr-graphene and graphene, showing the functionalization sites of benzene/Cr/graphene in the product η^6 -graphene/Cr/ η^6 -benzene. (b) TERS setup and the AFM images of (c) height and (d) phase, showing variations in the morphology. Scale bar: 1 μ m.

properties and is sensitive to variations in surface stiffness, adhesion, and composition. In Fig. 1(d), the graphene surface appears microscopically homogeneous, except for regions with steps and wrinkles. These wrinkles are likely due to the line defects of the underlying metal substrate, as confirmed by SEM images (Fig. S2).

The TERS measurements were performed along a 2 μ m line trace, with a step size of 20 nm, indicated by the dashed lines shown in Figs. 1(c) and 1(d). This region was chosen as relatively flat and featureless in the AFM maps, reducing the potential for artifacts in the spectroscopic mapping. Figure 2(a) shows the waterfall plot of TERS spectra measured along the line trace indicated. For clarity, these spectra are vector normalized in which the integral of each spectrum is set equal to 1. These TERS spectra exhibit the graphene G, D, and 2D bands consistently, but with spatially varying intensities. In addition to the graphene features, we can observe additional bands in the range of 1350–1580 cm^{-1} , between the G band and D band, which also exhibit spatially varying intensities and frequencies.

The D and G band regions of the selected spectra shown in Fig. 2(a) are expanded in panel b. The spectra exhibit the characteristic G bands at 1589 cm^{-1} of graphene [Fig. 2(b)], which is in good agreement with previous studies on crystalline monolayered graphene using TERS.^{31,33–36} The presence of the Raman-forbidden D band can be due to defects but also consistently appears in TERS of graphene due to the symmetry-breaking from plasmon mediation, as previously observed.^{31,33,35,47,48} The D band appears in a split form at 1318 and 1335 cm^{-1} in some spectra, as indicated by the dashed red lines. We attribute the appearance of the band at 1318 cm^{-1} to a D_1 band, originating from double resonance scattering of the electron by a phonon and then back-scattering by a defect.⁴⁹ We observe that the D band splitting is correlated with the additional peaks close to the G band. The intensity of D_1 is strongest with the presence of additional bands around 1550 cm^{-1} [Fig. 2(b)]. This correlation is indicative of an additional chemical contribution to graphene arising from localized functionalization.

Figure 2(c) shows a detailed view of the 2D band for the same selected spectra as panel b, to highlight the two sub-bands involved in the 2D envelope. Lorentzian peak fitting demonstrates that the peaks are asymmetric and have spatially varying intensities. The presence of sub-bands in the 2D band has been reported due to strain, doping, and the number of layers of graphene.^{50–52} As the sample is prepared with CVD, the changes in the relative intensity of I_{2D}/I_G and the presence of the 2D sub-bands may be related to regions of bilayer graphene, but this conclusion requires additional analysis of the correlations in spectral changes.

Inspection of the spectra reveals multiple complex variations across the line profile, with strong additional modes suggestive of functionalization. However, the positions of specific vibrational modes shift across the sample by up to 10 cm^{-1} , and their relative intensities and linewidths also vary. This behavior is common in TERS and is a consequence of the sensitivity of the enhancement to differences in tip-sample coupling or local environment,³³ in addition to the intrinsic heterogeneities appearing in the sample. These fluctuations can mask the underlying chemical changes of interest, requiring more advanced analytical techniques to probe correlations in spectral variations and their origin.

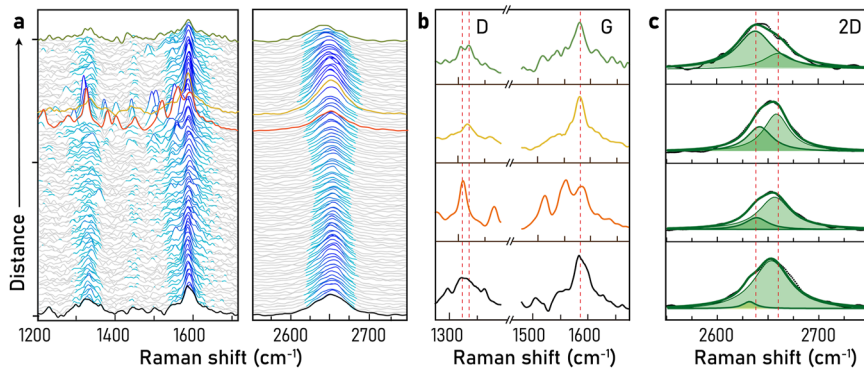


FIG. 2. (a) Stacked TERS from the line trace indicated in Figs. 1(c) and 1(d), showing the heterogeneous spectral shifts and linewidth in 2D bands. The sub-bands in D band are associated with the non-graphene features in the range of 1330–1590 cm^{-1} . Panels (b) and (c): the expanded TERS spectra at spots indicated in panel (a).

Chemical species identification via hyperspectral analysis

We, therefore, implement multivariate analysis, as previously employed to analyze hyperspectral imaging, such as stimulated Raman and TERS to extract chemical information.⁵³ In particular, we utilize vertex component analysis (VCA) to unmix the spectral components in TERS line scans. Standard spectral extraction techniques, such as principal component analysis (PCA), are often not suitable for TERS or samples without well-separated spectral components.^{54,55} PCA assumes linear separability and orthogonality of components, which is not always the case in complex hyperspectral data where spectral features overlap significantly. VCA, on the other hand, is designed to handle the challenges of hyperspectral data with overlapping spectral features. By isolating distinct spectral components, VCA provides detailed chemical information that is crucial for understanding the molecular composition and functional groups within the sample.

The data cube of a TERS image is preprocessed via spike removal, baseline correction, and normalization to make the spectra at each pixel comparable, thereby avoiding intensity variation effects. Next, we conduct VCA to identify significant spectral features. VCA works by decomposing the spectral data into their fundamental components, assuming that each spectrum is a combination of these underlying components. It projects unlabeled spectra into a simplified geometric space using singular value decomposition. The resulting VCA spectra [Fig. 3(a)] represent key features that capture most of the information from the original TERS data cube and can thus be used for general identification and characterization.

To guide the selection of the number of clusters to capture the features of our dataset, we calculate the spectral distance, which describes the degree of spectral similarity between spectra. The smaller the spectral distance, the more similar are the spectra. By calculating the spectral distance, we cluster spectra that are similar

to each other. The process involves repeatedly merging neighboring clusters based on their pairwise spectral distances, constructing a dendrogram of the dataset, as shown in Fig. S5. This dendrogram helps us determine the optimal number of clusters. We chose five components to reflect the spectral variation, capturing over 80% of the variance in the dataset (Fig. S5).

The extracted five TERS-VCA spectra from the TERS data cube of dimensionality 100×1600 are shown in Fig. 3(a). All the five components from n_1 to n_5 show a G band at 1589 cm^{-1} , in agreement with pristine graphene. The D band appears with three different types among the five components: a single D band (1335 cm^{-1}) in component n_1 , a single D_1 band (1318 cm^{-1}) in component n_4 and n_5 , and a split form containing both D and D_1 bands in components n_2 and n_3 .

The 2D band varies significantly in peak position in the component spectra due to changes in the relative intensity of sub-bands observed in the raw data [Fig. 2(c)]. Our observation of 2D sub-bands, G band, and split D bands from VCA-TERS spectra is consistent with those shown in Figs. 2(b) and 2(c), indicating that the multivariate analysis has captured the molecular features of the chemical components.

The n_1 component spectrum exhibits prominent graphene characteristics of D, G, and 2D bands. The intensity of $I_{2D}/I_G = 1.6$ suggests monolayer graphene.⁵² Components n_2 and n_3 appear similar in their spectral characteristics, including the I_{2D}/I_G ratio, appearance of split D bands, and weak additional features in the spectral range $1350\text{--}1580\text{ cm}^{-1}$. The I_{2D}/I_G ratio in both n_2 and n_3 is smaller than that of n_1 ($I_{2D}/I_G = 1.3$ and 1.2 for component n_2 and n_3 , respectively), implying bilayer graphene. The position of 2D sub-bands varies in components n_2 and n_3 , as presented in Table S1 of the fitting parameters. Component n_3 exhibits a 2D sub-band that is at lower frequency (2633 cm^{-1}) than that in component n_2 , suggesting n-type doping.⁴⁴ This behavior is consistent with the far-field Raman 2D band (Fig. S4), also attributed to functionalization doping.

Components n_4 and n_5 exhibit strong molecular signatures in the spectral range $1350\text{--}1580\text{ cm}^{-1}$. There are five spectral peaks observed at 1554 , 1505 , 1442 , 1399 , and 1374 cm^{-1} . The intensities of the five bands are correlated with the D_1 band, which is strong and well-defined. As the D_1 band is associated with short-range defects, we attribute the difference in n_4 compared to n_5 to the defect concentration, i.e., component n_4 exhibits a higher concentration of edge defects ($I_{D_1}/I_G > 1$) than component n_5 ($I_{D_1}/I_G < 1$).

We perform density functional theory (DFT) for mode assignments of the chemical species observed in the TERS-VCA components. The calculation is based on a $\text{Cr}(\eta^6\text{-C}_6\text{H}_6)$ complex attached to a monolayer graphene. The result shows that the planar structure of graphene remains unaffected, in agreement with the previously established molecular model.⁵⁶ The calculated spectrum of $(\eta^6\text{-graphene})\text{Cr}(\eta^6\text{-C}_6\text{H}_6)$, shown in Fig. 3(a), is generally in agreement with that of the VCA-TERS spectrum in the components n_4 and n_5 . The majority of functionalization bands appear near the D bands, likely due to the molecules introducing defects into the basal graphene structure. Assignment of the Raman bands of the five molecular vibrations is presented in Table I. We note differences in peak positions when comparing the VCA TERS with DFT models. These differences likely arise because the DFT model is an approximation of the actual graphene system, where the size

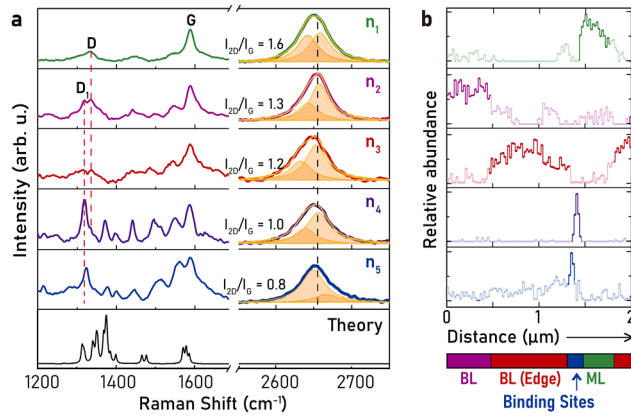


FIG. 3. (a) Extracted VCA spectra from the line trace shown in Fig. 2(a). Component n_1 (green) is assigned to pure monolayer graphene with metallic property; component n_2 (purple) is bilayer graphene; component n_3 (red) is edge state of bilayer graphene; and components n_4 and n_5 (dark and light blue, respectively) are $\text{Cr-C}_6\text{H}_6$ functionalized graphene. (b) The associated distribution of each component in panel (a).

TABLE I. Raman mode assignments observed in the TERS spectra shown in Fig. 3(a).

VCA-TERS	DFT	Assignment	Reference
1588	1586	Graphene G band	1591 ³⁵
1554	1578	(η^6 -graphene)Cr(η^6 -C ₆ H ₆)	
1505	1571	(η^6 -graphene)Cr(η^6 -C ₆ H ₆)	
1442	1477	(η^6 -graphene)Cr(η^6 -C ₆ H ₆)	
1399	1375	(η^6 -graphene)Cr(η^6 -C ₆ H ₆)	
1374	1350	(η^6 -graphene)Cr(η^6 -C ₆ H ₆)	
1335	1340	Graphene D band	1334, ³⁵ 1337 ⁴⁹
1319	1313	Graphene D ₁ band	1317 ⁴⁹

of the C-sp² plane can vary. In addition, the optical and mechanical stress introduced by TERS can cause TER spectra to have different peak positions than those calculated. However, the number of peaks and their general appearance are in good agreement. Thus, we attribute components n_4 and n_5 to the functionalization binding sites. There are weak but distinct peaks observed in the spectral range 1350–1580 cm⁻¹ in components n_2 and n_3 , which are also associated with molecular functionalization. The smaller intensity of the D sub-bands in n_2 and n_3 suggest a lower concentration of binding sites than those of n_4 and n_5 .

Defect-dependent molecular functionalization

The spatial distribution of each component across the 2 μm line profile, derived from non-negative least squares (NNLS) fitting, is shown in Fig. 3(b). The abundance profile shows how the TER spectra transition from one molecular domain to another. Each component is spatially well-separated, and through the VCA, it is possible to deduce that the functionalization sites (components n_4 and n_5) appear at the interface of pure monolayer graphene (n_1) and bilayer graphene (n_3). This observation is in good agreement with the previous reported correlation of binding sites with defective regions because of increased chemical reactivity on the graphene defect sites.⁵⁷ Near the zigzag edge state of bilayer graphene, the D-band has been observed to exhibit diminished intensity compared to that of the armchair edge state, as these edges support different phonon modes.⁵⁸ Similarly, Fig. 3(b) shows that component n_3 is distributed at the bilayer edge with the reduced D_1 and D bands [Fig. 3(a)].

The functionalization sites across components n_4 and n_5 can be considered as a structural defect at the graphene edge. Molecular Cr(η^6 -C₆H₆) has a tendency to bind at the edge of bilayer graphene, and component n_4 is shown to exist next to monolayer graphene (component n_1), with component n_5 on the opposite side toward the center of bilayer graphene. A lower I_{2D}/I_G ratio is associated with the graphene edge effect in components n_4 and n_5 , which has been observed previously.⁵⁹ We note that the lowered I_{2D}/I_G ratio could be associated with doping. As we prepared graphene using CVD, some regions of bilayer production are highly likely. In addition, the positions of the G and 2D bands in components n_4 and n_5 did not shift. We, therefore, attribute the varying I_{2D}/I_G ratio to the molecular binding on edges.

The binding regions cover 8 of 100 pixels, corresponding to a localization length of 160 nm. This observation is consistent with a prior study involving aryl-functionalization grafted graphene, where a charge localization length ranging from 45 to 125 nm was reported.¹⁶ Notably, we also observe a longer-range doping effect represented in component n_3 , which is distributed across a sub-micrometer distance next to the binding sites, implying that a low concentration of chemical functionalization can generate a doping effect through non-local electronic coupling.

To further characterize the spatial distribution of the attachment sites, we performed high-resolution TERS mapping over a small area to correlate with topographical data. Figure 4(a) shows a 100 \times 75 nm² AFM topography image, exhibiting topographic variations with height differences within 10 nm. Notably, the height distribution caused by the polycrystalline copper shown in Fig. 1(c), which is on the micrometer scale, is not dominant at this nanometer scale. The phase image shown in Fig. 4(b) confirms the absence of surface contamination as such contamination would typically cause dramatic shifts in the phase image.

TERS mapping was collected in the area shown in Figs. 4(a) and 4(b). The VCA workflow is particularly valuable for visualizing 2D spatial data cubes, where spatial correlations can be challenging to analyze compared to 1D line profiles. We applied VCA to the TERS image data cube (dimensions: 20 \times 15 \times 1600) to investigate the distribution of molecular species. For this sample, fewer components were required to capture 80% of the spectral variation, indicating a more spatially homogeneous chemical variation on the surface. (Figure S6).

The generated VCA spectra, shown in Fig. 4(c), exhibit similar chemical components as those shown in Fig. 3(a). The absence of molecular peaks in the spectral range 1350–1580 cm⁻¹ in component n_1 suggests pure graphene, similar to component n_1 shown in Fig. 3(a). The I_{2D}/I_G ratio of around 1.3 and the weaker D_1 band in component n_1 shown in Fig. 4(c) indicate pure bilayer graphene. Component n_2 exhibits a similar I_{2D}/I_G ratio to that of component

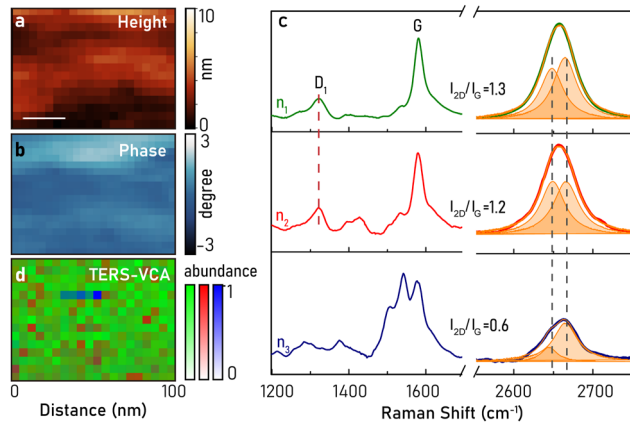


FIG. 4. (a) Height and phase image during TERS measurements. Scale bar: 20 nm. The extracted TERS-VCA spectra in the dot square location are shown in panel (b). Component n_1 (green) is assigned to pure bilayer graphene. Component n_2 (red) is the edge state. Component n_3 (blue) is assigned as functionalized graphene. (c) The abundance map of the three components.

n_1 [Fig. 4(b)], suggesting bilayer graphene with defects. The weak peaks in the spectral range 1350–1580 cm⁻¹ of component n_2 indicate weak molecular binding. The observation of molecular binding on bilayer graphene is consistent with that of components n_2 and n_3 shown in Fig. 3(a). Component n_3 suggests features of functionalization sites, similar to components n_4 and n_5 shown in Fig. 3(a). We observe a reduced I_{2D}/I_G ratio, which we attribute to molecular binding on edges. The diminished D and D_1 bands support the edge state in bilayer graphene.

The 2D spatial distribution of components is visualized in Fig. 4(d), showing clear domains in the TERS-VCA image. A uniform distribution of bilayer graphene covers the entire surface (indicated by green), while weak molecular binding sites are indicated in red. The closely spaced Cr(η^6 -C₆H₆) forms clustered functionalization sites (noted in blue), revealing local clusters with a size of ~20 nm. These clustered domains correlate with variations in the AFM height and phase diagrams.

In summary, Fig. 3(a) shows that a dense concentration of functional molecules induces strong and well-defined D_1 bands, likely due to the highly disordered graphene structure and high density of defects and edges. Conversely, Fig. 4(a) shows a spatially homogeneous surface with low defects and a more pristine graphene structure, distributed with weak molecular binding sites. Similar to how Clar's rule has been successfully used to predict coordination sites for chromium hexacarbonyls on small polycyclic aromatic hydrocarbons, this concept can be extended to graphene to predict "benzenoid" moieties. Our results suggest a strong correlation between existing defect sites and their reactivity toward functionalization on the graphene surface. As the basal plane of pristine graphene is chemically inert, the edges of bilayer and monolayer graphene serve as favored binding sites for molecules, as indicated by strong D_1 bands. This interfacial binding has been inaccessible in previous studies due to lack of simultaneous spatial and chemical sensitivity.

CONCLUSIONS

We have resolved the surface engineering of graphene through covalent surface modification, using chemically sensitive TERS imaging combined with VCA hyperspectral analysis. The hexahapto (η^6)-functionalization induces heterogeneous binding of the benzene–chromium molecular complex on the graphene surface, resulting in spatial variations of different species. The attachment of (C₆H₆)Cr(CO)₃ to the graphene surface through π -coordination with benzene rings forms (η^6 -C₆H₆)Cr moieties, where the chromium atom coordinates with the π electrons of the benzene ring in graphene. This interfacing retains the in-plane transport and sp² conjugation properties while introducing localized electronic states at the functionalization sites. With our analysis, we are able to separate contributions from pure monolayer graphene, bilayer graphene, edges, functionalization binding sites, and doping.

We find that the functionalizing molecules preferentially bind at intrinsic defects on the edges of layers of graphene. This result suggests that the homogeneity of graphene dictates the effectiveness of the bonding and controls the resulting device properties. Chemical vapor deposition (CVD) is considered the most promising method for industrial production of high-quality graphene, offering

low defects, good uniformity, and controlled layer numbers. Extending the CVD process to enable controlled η^6 -functionalization of graphene provides an easy and scalable approach for new applications in electronics, plasmonics, and beyond. We expect this work to open up the possibility of optimizing optoelectronic devices based on molecular-anchored 2D materials with the ability to translate complex, multicomponent spectral information into chemical knowledge.

SUPPLEMENTARY MATERIAL

The following file is available free of charge. The [supplementary material](#) provides further experimental details and information on analysis.

ACKNOWLEDGMENTS

This work was supported by the National Science Foundation Chemical Measurement and Imaging program, under Grant No. CHE-1848278. Part of this work was performed at the Chapel Hill Nanofabrication and Analysis Laboratory, a member of the North Carolina Research Triangle Nanotechnology Network (RTNN), which is supported by the National Science Foundation, Grant No. ECCS-1542015, as part of the National Nanotechnology Coordinated Infrastructure (NNCI).

AUTHOR DECLARATIONS

Conflict of Interest

The authors have no conflicts to disclose.

Author Contributions

X.Y. and C.-W.H. contributed equally to this work.

Xiao You: Conceptualization (equal); Data curation (lead); Formal analysis (equal); Investigation (equal); Methodology (equal); Software (supporting); Validation (equal); Visualization (equal); Writing – original draft (equal); Writing – review & editing (equal).

Chiung-Wei Huang: Conceptualization (equal); Data curation (supporting); Formal analysis (equal); Investigation (equal); Methodology (equal); Software (equal); Validation (equal); Visualization (equal); Writing – original draft (equal); Writing – review & editing (equal).

Kizhanipuram Vinodgopal: Conceptualization (equal); Data curation (supporting); Formal analysis (supporting); Funding acquisition (supporting); Investigation (supporting); Methodology (equal); Resources (supporting); Validation (equal); Writing – original draft (supporting); Writing – review & editing (supporting).

Joanna M. Atkin: Conceptualization (lead); Formal analysis (supporting); Funding acquisition (lead); Investigation (lead); Methodology (supporting); Project administration (lead); Resources (lead); Software (supporting); Supervision (lead); Validation (supporting); Visualization (equal); Writing – original draft (supporting); Writing – review & editing (lead).

DATA AVAILABILITY

The experimental data and code that support the findings of this study are available from JMA on reasonable request.

REFERENCES

- ¹Y. M. Lin, C. Dimitrakopoulos, K. A. Jenkins, D. B. Farmer, H. Y. Chiu, A. Grill, and P. Avouris, "100-GHz transistors from wafer-scale epitaxial graphene," *Science* **327**, 662 (2010).
- ²K. Kim, J.-Y. Choi, T. Kim, S.-H. Cho, and H.-J. Chung, "A role for graphene in silicon-based semiconductor devices," *Nature* **479**, 338–344 (2011).
- ³D. Rodrigo, O. Limaj, D. Janner, D. Etezadi, F. J. García de Abajo, V. Pruneri, and H. Altug, "Mid-infrared plasmonic biosensing with graphene," *Science* **349**, 165 (2015).
- ⁴Z. Wang, S. Wu, L. Colombi Ciacchi, and G. Wei, "Graphene-based nanoplatforms for surface-enhanced Raman scattering sensing," *Analyst* **143**, 5074–5089 (2018).
- ⁵T. Yokoyama, T. Tanaka, Y. Shimokawa, R. Yamachi, Y. Saito, and K. Uchida, "Pd-functionalized, suspended graphene nanosheet for fast, low-energy multimolecular sensors," *ACS Appl. Nano Mater.* **1**, 3886–3894 (2018).
- ⁶G. Reina, J. M. González-Domínguez, A. Criado, E. Vázquez, A. Bianco, and M. Prato, "Promises, facts and challenges for graphene in biomedical applications," *Chem. Soc. Rev.* **46**, 4400–4416 (2017).
- ⁷T. Mueller, F. Xia, and P. Avouris, "Graphene photodetectors for high-speed optical communications," *Nat. Photonics* **4**, 297–301 (2010).
- ⁸S. K. Behura, C. Wang, Y. Wen, and V. Berry, "Graphene–semiconductor heterojunction sheds light on emerging photovoltaics," *Nat. Photonics* **13**, 312–318 (2019).
- ⁹F. Xia, D. B. Farmer, Y.-M. Lin, and P. Avouris, "Graphene field-effect transistors with high on/off current ratio and large transport band gap at room temperature," *Nano Lett.* **10**, 715–718 (2010).
- ¹⁰S. J. Zhang, S. S. Lin, X. Q. Li, X. Y. Liu, H. A. Wu, W. L. Xu, P. Wang, Z. Q. Wu, H. K. Zhong, and Z. J. Xu, "Opening the band gap of graphene through silicon doping for the improved performance of graphene/GaAs heterojunction solar cells," *Nanoscale* **8**, 226–232 (2016).
- ¹¹J. Wang, F. Ma, W. Liang, R. Wang, and M. Sun, "Optical, photonic and optoelectronic properties of graphene, h-BN and their hybrid materials," *Nanophotonics* **6**, 943–976 (2017).
- ¹²G. Yang, L. Li, W. B. Lee, and M. C. Ng, "Structure of graphene and its disorders: A review," *Sci. Technol. Adv. Mater.* **19**, 613–648 (2018).
- ¹³K.-J. Jeon, Z. Lee, E. Pollak, L. Moreschini, A. Bostwick, C.-M. Park, R. Mendelsberg, V. Radmilovic, R. Kostecki, T. J. Richardson, and E. Rotenberg, "Fluorographene: A wide bandgap semiconductor with ultraviolet luminescence," *ACS Nano* **5**, 1042–1046 (2011).
- ¹⁴C.-K. Chang *et al.*, "Band gap engineering of chemical vapor deposited graphene by *in Situ* BN doping," *ACS Nano* **7**, 1333–1341 (2013).
- ¹⁵C. Lin, Y. Feng, Y. Xiao, M. Dürr, X. Huang, X. Xu, R. Zhao, E. Wang, X.-Z. Li, and Z. Hu, "Direct observation of ordered configurations of hydrogen adatoms on graphene," *Nano Lett.* **15**, 903–908 (2015).
- ¹⁶H. Zhang, E. Bekyarova, J.-W. Huang, Z. Zhao, W. Bao, F. Wang, R. C. Haddon, and C. N. Lau, "Aryl functionalization as a route to band gap engineering in single layer graphene devices," *Nano Lett.* **11**, 4047–4051 (2011).
- ¹⁷S. Sarkar, E. Bekyarova, S. Niyogi, and R. C. Haddon, "Diels–Alder chemistry of graphite and graphene: Graphene as diene and dienophile," *J. Am. Chem. Soc.* **133**, 3324–3327 (2011).
- ¹⁸S. Niyogi, E. Bekyarova, M. E. Itkis, H. Zhang, K. Shepperd, J. Hicks, M. Sprinkle, C. Berger, C. N. Lau, W. A. deHeer, E. H. Conrad, and R. C. Haddon, "Spectroscopy of covalently functionalized graphene," *Nano Lett.* **10**, 4061–4066 (2010).
- ¹⁹V. Georgakilas, M. Otyepka, A. B. Bourlinos, V. Chandra, N. Kim, K. C. Kemp, P. Hobza, R. Zboril, and K. S. Kim, "Functionalization of graphene: Covalent and non-covalent approaches, derivatives and applications," *Chem. Rev.* **112**, 6156–6214 (2012).
- ²⁰T. S. Sreeprasad and V. Berry, "How do the electrical properties of graphene change with its functionalization?" *Small* **9**, 341–350 (2013).
- ²¹J. Li, M. Li, L.-L. Zhou, S.-Y. Lang, H.-Y. Lu, D. Wang, C.-F. Chen, and L.-J. Wan, "Click and patterned functionalization of graphene by Diels–Alder reaction," *J. Am. Chem. Soc.* **138**, 7448–7451 (2016).
- ²²H. Zhu, P. Huang, L. Jing, T. Zuo, Y. Zhao, and X. Gao, "Microstructure evolution of diazonium functionalized graphene: A potential approach to change graphene electronic structure," *J. Mater. Chem.* **22**, 2063–2068 (2012).
- ²³S. Sarkar, H. Zhang, J.-W. Huang, F. Wang, E. Bekyarova, C. N. Lau, and R. C. Haddon, "Organometallic hexahapto functionalization of single layer graphene as a route to high mobility graphene devices," *Adv. Mater.* **25**, 1131–1136 (2013).
- ²⁴A. Pekker, M. Chen, E. Bekyarova, and R. C. Haddon, "Photochemical generation of bis-hexahapto chromium interconnects between the graphene surfaces of single-walled carbon nanotubes," *Mater. Horiz.* **2**, 81–85 (2015).
- ²⁵M. Chen, A. Pekker, W. Li, M. E. Itkis, R. C. Haddon, and E. Bekyarova, "Organometallic chemistry of graphene: Photochemical complexation of graphene with group 6 transition metals," *Carbon* **129**, 450–455 (2018).
- ²⁶S. Che, S. K. Behura, and V. Berry, "Photo-organometallic, nanoparticle nucleation on graphene for cascaded doping," *ACS Nano* **13**, 12929–12938 (2019).
- ²⁷I. Kalinina, E. Bekyarova, S. Sarkar, F. Wang, M. E. Itkis, X. Tian, S. Niyogi, N. Jha, and R. C. Haddon, "Hexahapto-metal complexes of single-walled carbon nanotubes," *Macromol. Chem. Phys.* **213**, 1001–1019 (2012).
- ²⁸S. Che, K. Jasuja, S. K. Behura, P. Nguyen, T. S. Sreeprasad, and V. Berry, "Retained carrier-mobility and enhanced plasmonic-photovoltaics of graphene via ring-centered η^6 functionalization and nanointerfacing," *Nano Lett.* **17**, 4381–4389 (2017).
- ²⁹H. Lim, J. S. Lee, H.-J. Shin, H. S. Shin, and H. C. Choi, "Spatially resolved spontaneous reactivity of diazonium salt on edge and basal plane of graphene without surfactant and its doping effect," *Langmuir* **26**, 12278–12284 (2010).
- ³⁰P. Ramesh, M. E. Itkis, E. Bekyarova, F. Wang, S. Niyogi, X. Chi, C. Berger, W. de Heer, and R. C. Haddon, "Electro-oxidized epitaxial graphene channel field-effect transistors with single-walled carbon nanotube thin film gate electrode," *J. Am. Chem. Soc.* **132**, 14429–14436 (2010).
- ³¹W. Su, N. Kumar, N. Dai, and D. Roy, "Nanoscale mapping of intrinsic defects in single-layer graphene using tip-enhanced Raman spectroscopy," *Chem. Commun.* **52**, 8227–8230 (2016).
- ³²W. Su, N. Kumar, A. Krayev, and M. Chaigneau, "In situ topographical chemical and electrical imaging of carboxyl graphene oxide at the nanoscale," *Nat. Commun.* **9**, 2891 (2018).
- ³³K.-D. Park, M. B. Raschke, J. M. Atkin, Y. H. Lee, and M. S. Jeong, "Probing bilayer grain boundaries in large-area graphene with tip-enhanced Raman spectroscopy," *Adv. Mater.* **29**, 1603601 (2017).
- ³⁴R. Beams, "Tip-enhanced Raman scattering of graphene," *J. Raman Spectrosc.* **49**, 157–167 (2018).
- ³⁵M. V. Balois, N. Hayazawa, S. Yasuda, K. Ikeda, B. Yang, E. Kazuma, Y. Yokota, Y. Kim, and T. Tanaka, "Visualization of subnanometric phonon modes in a plasmonic nano-cavity via ambient tip-enhanced Raman spectroscopy," *npj 2D Mater. Appl.* **3**, 38 (2019).
- ³⁶A. C. Gadelha *et al.*, "Localization of lattice dynamics in low-angle twisted bilayer graphene," *Nature* **590**, 405–409 (2021).
- ³⁷X. You, S. Maharjan, K. Vinodgopal, and J. M. Atkin, "Nanoscale insights into graphene oxide reduction by tip-enhanced Raman spectroscopy," *Phys. Chem. Chem. Phys.* **26**, 9871 (2024).
- ³⁸D. A. Sokolov, K. R. Shepperd, and T. M. Orlando, "Formation of graphene features from direct laser-induced reduction of graphite oxide," *J. Phys. Chem. Lett.* **1**, 2633–2636 (2010).
- ³⁹M. P. McDonald, A. Eltom, F. Vietmeyer, J. Thapa, Y. V. Morozov, D. A. Sokolov, J. H. Hodak, K. Vinodgopal, P. V. Kamat, and M. Kuno, "Direct observation of spatially heterogeneous single-layer graphene oxide reduction kinetics," *Nano Lett.* **13**, 5777–5784 (2013).
- ⁴⁰E. Bekyarova, S. Sarkar, F. Wang, M. E. Itkis, I. Kalinina, X. Tian, and R. C. Haddon, "Effect of covalent chemistry on the electronic structure and properties of carbon nanotubes and graphene," *Acc. Chem. Res.* **46**, 65–76 (2013).

- ⁴¹X. Tian, S. Sarkar, M. L. Moser, F. Wang, A. Pekker, E. Bekyarova, M. E. Itkis, and R. C. Haddon, "Effect of group 6 transition metal coordination on the conductivity of graphite nanoplatelets," *Mater. Lett.* **80**, 171–174 (2012).
- ⁴²X. Li, W. Cai, J. An, S. Kim, J. Nah, D. Yang, R. Piner, A. Velamakanni, I. Jung, E. Tutuc, S. K. Banerjee, L. Colombo, and R. S. Ruoff, "Large-area synthesis of high-quality and uniform graphene films on copper foils," *Science* **324**, 1312 (2009).
- ⁴³J.-B. Wu, M.-L. Lin, X. Cong, H.-N. Liu, and P.-H. Tan, "Raman spectroscopy of graphene-based materials and its applications in related devices," *Chem. Soc. Rev.* **47**, 1822–1873 (2018).
- ⁴⁴B. Tang, H. Guoxin, and H. Gao, "Raman spectroscopic characterization of graphene," *Appl. Spectrosc. Rev.* **45**, 369–407 (2010).
- ⁴⁵G. Wang *et al.*, "Seamless lateral graphene p-n junctions formed by selective in situ doping for high-performance photodetectors," *Nat. Commun.* **9**, 5168 (2018).
- ⁴⁶K. Sampathkumar, V. Diez-Cabanes, P. Kovaricek, E. del Corro, M. Bouša, J. Hošek, M. Kalbac, and O. Frank, "On the suitability of Raman spectroscopy to monitor the degree of graphene functionalization by diazonium salts," *J. Phys. Chem. C* **123**, 22397–22402 (2019).
- ⁴⁷P. Wang, D. Zhang, L. Li, Z. Li, L. Zhang, and Y. Fang, "Reversible defect in graphene investigated by tip-enhanced Raman spectroscopy," *Plasmonics* **7**, 555–561 (2012).
- ⁴⁸K. Ikeda, M. Takase, N. Hayazawa, S. Kawata, K. Murakoshi, and K. Uosaki, "Plasmonically nanoconfined light probing invisible phonon modes in defect-free graphene," *J. Am. Chem. Soc.* **135**, 11489–11492 (2013).
- ⁴⁹Z. Luo, C. Cong, J. Zhang, Q. Xiong, and T. Yu, "The origin of sub-bands in the Raman D-band of graphene," *Carbon* **50**, 4252–4258 (2012).
- ⁵⁰O. Frank, M. Mohr, J. Maultzsch, C. Thomsen, I. Riaz, R. Jalil, K. S. Novoselov, G. Tsoukleri, J. Parthenios, K. Papagelis, L. Kavan, and C. Galiotis, "Raman 2D-band splitting in graphene: Theory and experiment," *ACS Nano* **5**, 2231–2239 (2011).
- ⁵¹J. A. Robinson, M. Wetherington, J. L. Tedesco, P. M. Campbell, X. Weng, J. Stitt, M. A. Fanton, E. Frantz, D. Snyder, B. L. VanMil, G. G. Jernigan, R. L. Myers-Ward, C. R. Eddy, and D. K. Gaskill, "Correlating Raman spectral signatures with carrier mobility in epitaxial graphene: A guide to achieving high mobility on the wafer scale," *Nano Lett.* **9**, 2873–2876 (2009).
- ⁵²Y. Hao, Y. Wang, L. Wang, Z. Ni, Z. Wang, R. Wang, C. K. Koo, Z. Shen, and J. T. L. Thong, "Probing layer number and stacking order of few-layer graphene by Raman spectroscopy," *Small* **6**, 195–200 (2010).
- ⁵³H. Shinzawa, K. Awa, W. Kanematsu, and Y. Ozaki, "Multivariate data analysis for Raman spectroscopic imaging," *J. Raman Spectrosc.* **40**, 1720–1725 (2009).
- ⁵⁴A. Alfonso-Garcia, J. Paugh, M. Farid, S. Garg, J. V. Jester, and E. O. Potma, "A machine learning framework to analyze hyperspectral stimulated Raman scattering microscopy images of expressed human meibum," *J. Raman Spectrosc.* **48**, 803–812 (2017).
- ⁵⁵S. Jiang, X. Zhang, Y. Zhang, C. Hu, R. Zhang, Y. Zhang, Y. Liao, Z. J. Smith, Z. Dong, and J. G. Hou, "Subnanometer-resolved chemical imaging via multivariate analysis of tip-enhanced Raman maps," *Light Sci. Appl.* **6**, e17098 (2017).
- ⁵⁶I. P. Gloriov, R. Marchal, J.-Y. Saillard, and Y. F. Oprunenko, "Chromium tricarbonyl and chromium benzene complexes of graphene, their properties, stabilities, and inter-ring haptotropic rearrangements—A DFT investigation," *Eur. J. Inorg. Chem.* **2015**, 250–257.
- ⁵⁷J. Hong, J.-B. Lee, S. Lee, J. Seo, H. Lee, J. Y. Park, J.-H. Ahn, T. Il Seo, T. Lee, and H.-B.-R. Lee, "A facile method for the selective decoration of graphene defects based on a galvanic displacement reaction," *NPG Asia Mater.* **8**, e262 (2016).
- ⁵⁸M. Begliarbekov, O. Sul, S. Kalliakos, E.-H. Yang, and S. Strauf, "Determination of edge purity in bilayer graphene using μ -Raman spectroscopy," *Appl. Phys. Lett.* **97**, 031908 (2010).
- ⁵⁹W. Su and D. Roy, "Visualizing graphene edges using tip-enhanced Raman spectroscopy," *J. Vac. Sci. Technol., B: Nanotechnol. Microelectron.: Mater., Process., Meas., Phenom.* **31**, 041808 (2013).